JOURNAL OF AIRCRAFT
Vol. 32, No. 5, September–October 1995

Aeroelastic Actuation Using Elastic and Induced Strain Anisotropy

Charrissa Y. Lin* and Edward F. Crawley†
Massachusetts Institute of Technology, Cambridge, Massachusetts 02139

The effects of elastic anisotropy, induced strain anisotropy, and geometric sweep on piezoelectric aeroelastic authority are studied via a hybrid Ritz-typical section. The governing parameters for piezoelectric actuation are determined: the piezoelectric authority parameter, the piezoelectric induced strain anisotropy, and the piezoelectric angle. Three distinct piezoelectric actuators are introduced: 1) an isotropic actuator, 2) a "bend" anisotropic actuator, and 3) a "twist" anisotropic actuator. Open- and closed-loop analyses are conducted to compare the relative authority of the three piezoelectric actuators and a trailing-edge flap. A combination piezoelectric actuator is introduced that provides the best overall performance.

I. Introduction

THE use of direct strain actuators such as piezoelectrics for aeroelastic control has generated great interest in the aeroelastic community. Lazarus et al.[1] described the fundamental mechanisms of strain-actuated aeroelastic control. Small-scale experiments have been conducted[2,3] and larger scale wind-tunnel tests are underway.[4] The piezoelectric actuators used in these models are thin-sheet piezoelectrics, which are in-plane isotropic both in their elastic and induced strain properties. Due to this isotropy there is no direct method for these actuators to induce wing torsion. However, control over angle of attack is found to be essential in high authority aeroelastic control.[1]

The objective of this article is to qualitatively examine the effectiveness of three different methods for enabling piezoelectric aeroelastic control, specifically focusing on torsional control. These methods include tailoring the anisotropic composite laminate, utilizing anisotropic thin-sheet piezoelectrics, and geometrically sweeping the wing. The comparisons are made via a hybrid Ritz-typical section model that includes these physical phenomena.

Using a tailored anisotropic composite laminate provides the designer with potentially beneficial elastic coupling mechanisms. The aeroelastic benefit of altering flutter and divergence speeds of passively tailored composites is already well understood.[5,6] Through the use of extension- and bend-twist coupling mechanisms, tailored laminates enable torsional authority from isotropic piezoelectrics. Because changes in the operational thermal environment induce undesirable twist in nonsymmetric extension-twist laminates, bend-twist coupled laminates are more promising.

A second method of torsional control involves anisotropic piezoelectrics. Piezoelectric or induced strain anisotropy refers to piezoelectrics that exhibit a larger induced strain along one in-plane axis, the piezoelectric major axis, than along the other axis, the piezoelectric minor axis. Anisotropic piezoelectrics have been developed recently using piezoelectric fiber composites,[7] interdigitated electrodes,[8] and directionally attached piezoelectrics.[9] The anisotropic nature can be exploited by aligning the piezoelectric major axis to create extensional strain at an angle to the elastic axis and induce torsion in the structure.

By geometrically sweeping the wing, coupling between structural bending and aerodynamic angle of attack is created. In addition to the effect on the passive aeroelastic behavior, this coupling mechanism provides a means of piezoelectric authority on angle of attack. Ehlers and Weisshaar's study on flexural axis control utilizes this coupling mechanism.[10]

These three methods are modeled and incorporated into a hybrid Ritz-typical section model. The model uses a Rayleigh–Ritz analysis of an anisotropic plate with piezoelectric actuators to obtain expressions for the bending and torsion spring constants of a typical section as well as the piezoelectric actuation expressions. Initially, their effects on passive aeroelastic behavior are examined. Next, the open-loop effectiveness of the piezoelectrics and a flap on both plunge and pitch is studied for varying composite fiber angle and piezoelectric angle at zero airspeed and at a nominal airspeed below divergence. The final section compares the performance of controllers designed using isotropic piezoelectrics, anisotropic piezoelectrics, and a flap.

II. Typical Section Model

The geometry of the typical section can be seen in Fig. 1. The two section degrees of freedom are pitch α and plunge h. The forces acting on this section include those due to strain actuators and those due to the basic wing- and flap-induced aerodynamics.

The three coupling mechanisms are incorporated into the typical section. First, the anisotropy of a laminated structure is modeled using a Ritz analysis. Expressions for the uncoupled bending and torsional stiffnesses per unit span K_h and K_α and elastic axis location ab of the typical section are derived. Second, the steady aerodynamics associated with geo-

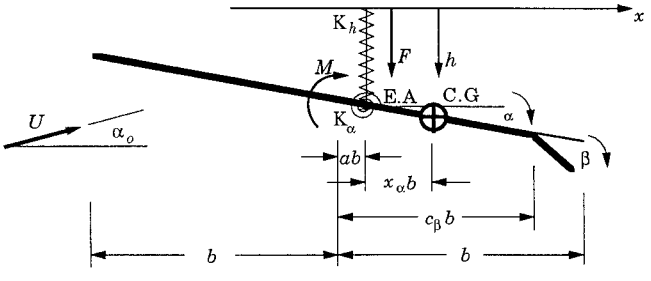

Fig. 1 Typical section geometry.

Presented as Paper 94-1386 at the AIAA 35th Structures, Structural Dynamics, and Materials Conference, Hilton Head, SC, April 18–20, 1994; received May 11, 1994; revision received March 18, 1995; accepted for publication March 20, 1995.

*Graduate Research Assistant. Student Member AIAA.
†Professor of Aeronautics and Astronautics and MacVicar Faculty Fellow. Fellow AIAA.

metric sweep are included and transformed to the elastic axis location. The trailing-edge flap β is modeled as a rigid surface with no inertial dynamics. Third, piezoelectrics that are anisotropic in their elastic and induced strain properties are modeled using a Ritz analysis, and expressions for their equivalent forces and moments at the elastic axis are derived.

A. Modeling of the Elastic Anisotropy

The wing is modeled as an anisotropic plate. Using energy methods, the governing differential equation for an anisotropic plate with induced strain actuation is derived as[11]

$$D_{11}\frac{\partial^4 w}{\partial x^4} + 2D_{12}\frac{\partial^4 w}{\partial x^2 \partial y^2} + 4D_{16}\frac{\partial^4 w}{\partial x^3 \partial y} + D_{22}\frac{\partial^4 w}{\partial y^4} + 4D_{26}\frac{\partial^4 w}{\partial x \partial y^3} + 4D_{66}\frac{\partial^4 w}{\partial x^2 \partial y^2} + \frac{\partial^2 m_{\Lambda_{11}}}{\partial x^2} + \frac{\partial^2 m_{\Lambda_{12}}}{\partial x^2} + \frac{\partial^2 m_{\Lambda_{21}}}{\partial y^2} + \frac{\partial^2 m_{\Lambda_{22}}}{\partial y^2} = \Delta p_A \tag{1}$$

where

$$D_{ij} = \int \bar{Q}_{ij} z^2 \, dz$$

$$m_{\Lambda_{ij}} = \int \bar{Q}_{ij} \Lambda_j z \, dz$$

and Λ_j is the actuation strain in the j direction and $\bar{Q}_{ij}$ is the modulus (where 1, 2 correspond to x, y). Note that the integral expression for $m_{\Lambda_{ij}}$ includes only the ijth term without a summation on j.

In order to derive expressions for the two spring constants K_h and K_α and the nondimensional elastic axis location a, a two-mode Rayleigh–Ritz approach is used. All structural modeling is completed in the $\bar{x}$, $\bar{y}$ system (Fig. 2) (overbar indicates dimensions in the $\bar{x}$, $\bar{y}$ system). The two Ritz modes are a bending mode, parabolic in the spanwise direction, and a linear twist mode

$$w(\bar{x}, \bar{y}, t) = \sum_{i=1}^{2} \gamma_i(\bar{x}, \bar{y}) q_i(t)$$

$$\gamma_1(\bar{x}, \bar{y}) = \frac{\bar{x}^2}{\bar{l}_{ts}^2} = \frac{16\bar{x}^2}{9\bar{l}^2} \tag{2}$$

$$\gamma_2(\bar{x}, \bar{y}) = \frac{\bar{x}}{\bar{l}_{ts}}\bar{y} = \frac{4\bar{x}}{3\bar{l}}\bar{y}$$

where $\bar{l}_{ts}$ is the spanwise distance to the typical section. When evaluated at the three-quarter span, the mode shapes of Eq. (2) produce unit bending deflection and unit structural twist at the midchord, here used as a reference point (denoted by the subscript c):

$$\bar{h}_c(t) = w(\bar{l}_{ts}, 0, t) = q_1(t)$$

$$\frac{\partial \bar{h}_c}{\partial \bar{y}} = \bar{\alpha}_c(t) = \frac{\partial w}{\partial \bar{y}}(\bar{l}_{ts}, 0, t) = q_2(t) \tag{3}$$

The shapes of Eq. (2) are differentiated to obtain strain mode shapes and then incorporated into the strain energy expression with the appropriate elastic moduli to obtain the structural stiffness matrix, which includes the passive stiffness of any piezoelectrics present

$$\begin{Bmatrix} \bar{F}_c \bar{l} \\ \bar{M}_c \bar{l} \end{Bmatrix} = \begin{bmatrix} \frac{8\bar{l}\bar{b}}{\bar{l}_{ts}^4} D_{11} & \frac{8\bar{l}\bar{b}}{\bar{l}_{ts}^3} D_{16} \\ \frac{8\bar{l}\bar{b}}{\bar{l}_{ts}^3} D_{16} & \frac{8\bar{l}\bar{b}}{\bar{l}_{ts}^2} D_{66} \end{bmatrix} \begin{Bmatrix} q_1 \\ q_2 \end{Bmatrix} = Kq \tag{4}$$

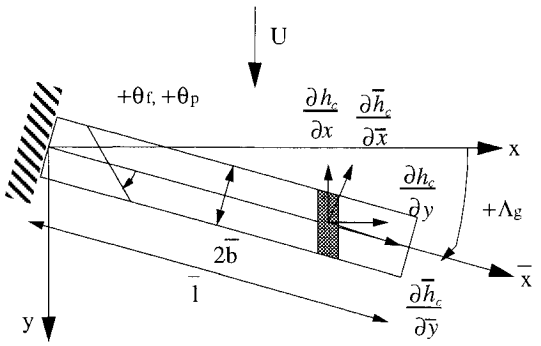

Fig. 2 Sign convention for the swept-wing model showing structural ($\bar{x}$, $\bar{y}$) and flowwise (x, y) axes.

where $\bar{F}_c$ and $\bar{M}_c$ are the load and moment per span at the midchord of the typical section.

To incorporate this coupled stiffness matrix into the typical section model, the elastic axis location and corresponding uncoupled stiffness (per unit span) matrix must be found. The transformation between the displacements at the midchord and at the elastic axis is

$$\begin{Bmatrix} q_1 \\ q_2 \end{Bmatrix} = \begin{Bmatrix} \bar{h}_c \\ \bar{\alpha}_c \end{Bmatrix} = \begin{bmatrix} 1 & -a\bar{b} \\ 0 & 1 \end{bmatrix} \begin{Bmatrix} \bar{h}_{EA} \\ \bar{\alpha}_{EA} \end{Bmatrix} = T_{EA} \begin{Bmatrix} \bar{h}_{EA} \\ \bar{\alpha}_{EA} \end{Bmatrix} \tag{5}$$

The spring forces per unit span at the elastic axis are calculated by dividing Eq. (4) by the span $\bar{l}$, and appropriate use of the transform matrix T_{EA} [see Eq. (5)]:

$$\begin{Bmatrix} \bar{F}_{EA} \\ \bar{M}_{EA} \end{Bmatrix} = \left(\frac{1}{\bar{l}}\right) T_{EA}^T K T_{EA} \begin{Bmatrix} \bar{h}_{EA} \\ \bar{\alpha}_{EA} \end{Bmatrix} \tag{6}$$

The location of the elastic axis and the uncoupled stiffnesses are found by setting the off-diagonal terms of $T_{EA}^T K T_{EA}$ to zero:

$$a = \frac{K_{12}}{K_{11}\bar{b}} = \frac{3}{4}\frac{\bar{l}}{\bar{b}}\frac{D_{16}}{D_{11}}$$

$$K_h = \frac{K_{11}}{\bar{l}} = \frac{8\bar{b}}{\bar{l}_{ts}^4} D_{11} \tag{7}$$

$$K_\alpha = \frac{K_{22}}{\bar{l}}\left(1 - \frac{K_{12}^2}{K_{11}K_{22}}\right) = \frac{8\bar{b}}{\bar{l}_{ts}^2} D_{66}\left(1 - \frac{D_{16}^2}{D_{11}D_{66}}\right)$$

In this simple model, the elastic axis is directly related to the ratio of bending-torsion coupling to spanwise stiffness.

B. Modeling of the Aerodynamic Operators

Since the typical section is taken in the structural coordinates, the aerodynamic model, developed in flowwise coordinates, must be transformed. Steady aerodynamic forces are used to simplify the expressions and to focus on the fundamental trends involved in the use of piezoelectric actuation. For a straight wing ($\Lambda_g = 0$), the static aerodynamic forces are only due to the twist angle α_c, since it is synonymous with the angle of attack in this case. The inclusion of aerodynamic forces for a straight wing introduces twist-bend coupling: when the wing twists, the lift force created bends the wing.

There are several corrections to the aerodynamic forces that must be made for the incorporation of geometric sweep angle Λ_g (Fig. 2). First, a cos Λ_g correction on the lift-curve slope must be made. Second, the geometry of the typical section is altered. Spanwise dimensions are shortened and chordwise dimensions are lengthened. Equations (8) and (9) give the

aerodynamic forces in the flowwise axes with the geometrical modifications and the correction of the lift-curve slope:

$$\begin{Bmatrix} F_c \\ M_{c_y} \\ M_{c_x} \end{Bmatrix} = A \begin{Bmatrix} \bar{h}_c \\ \dfrac{\partial \bar{h}_c}{\partial x} \\ \dfrac{\partial \bar{h}_c}{\partial y} \end{Bmatrix} = A \begin{Bmatrix} \bar{h}_c \\ \dfrac{\partial \bar{h}_c}{\partial x} \\ \alpha_c \end{Bmatrix} \tag{8}$$

$$A = \begin{bmatrix} 0 & 0 & -\rho U^2(\bar{b}/\cos\Lambda_g)(C_{L_\alpha}\cos\Lambda_g)(\Delta\bar{x}\cos\Lambda_g) \\ 0 & 0 & 0 \\ 0 & 0 & \rho U^2(\bar{e}/\cos\Lambda_g)(\bar{b}/\cos\Lambda_g)(C_{L_\alpha}\cos\Lambda_g)(\Delta\bar{x}\cos\Lambda_g) \end{bmatrix} \tag{9}$$

Finally, the aerodynamic forces must be transformed from the flowwise axes x, y to the structural axes $\bar{x}$, $\bar{y}$ (Fig. 2).

$$\begin{Bmatrix} \bar{h}_c \\ \dfrac{\partial \bar{h}_c}{\partial x} \\ \dfrac{\partial \bar{h}_c}{\partial y} \end{Bmatrix} = \begin{bmatrix} 1 & 0 & 0 \\ 0 & \cos\Lambda_g & -\sin\Lambda_g \\ 0 & \sin\Lambda_g & \cos\Lambda_g \end{bmatrix} \begin{Bmatrix} \bar{h}_c \\ \dfrac{\partial \bar{h}_c}{\partial \bar{x}} \\ \dfrac{\partial \bar{h}_c}{\partial \bar{y}} \end{Bmatrix}$$

$$= T_{\Lambda_g} \begin{Bmatrix} \bar{h}_c \\ \dfrac{\partial \bar{h}_c}{\partial \bar{x}} \\ \dfrac{\partial \bar{h}_c}{\partial \bar{y}} \end{Bmatrix} \tag{10}$$

The inclusion of geometric sweep introduces bend-twist coupling in contrast to the twist-bend coupling of the unswept aerodynamic forces. When the wing is bent, there is no twist in the structural axes, but in the flowwise axes, the wing has an angle of attack.

The typical section equations of motion have only two degrees of freedom: 1) a plunge motion q_1 and 2) a pitch motion q_2. The displacement and slopes on the right-hand side (RHS) of Eq. (10) must be expressed in terms of these two degrees of freedom, and the generalized aerodynamic forces on these two degrees of freedom must be found. Recalling Eq. (3), the appropriate transformation matrix is

$$\begin{Bmatrix} \bar{h}_c \\ \dfrac{\partial \bar{h}_c}{\partial \bar{x}} \\ \dfrac{\partial \bar{h}_c}{\partial \bar{y}} \end{Bmatrix} = \begin{bmatrix} \gamma_1(\bar{l}_{ts}, 0, t) & 0 \\ \dfrac{\partial \gamma_1}{\partial \bar{x}}(\bar{l}_{ts}, 0, t) & 0 \\ 0 & \dfrac{\partial \gamma_2}{\partial \bar{y}}(\bar{l}_{ts}, 0, t) \end{bmatrix} \begin{Bmatrix} q_1 \\ q_2 \end{Bmatrix}$$

$$= T_M \begin{Bmatrix} q_1 \\ q_2 \end{Bmatrix} \tag{11}$$

Consequently, the generalized aerodynamic forces acting at the midchord in the structural axes are

$$\begin{Bmatrix} Q_1 \\ Q_2 \end{Bmatrix} = T_M^T T_{\Lambda_g}^T A T_{\Lambda_g} T_M \begin{Bmatrix} q_1 \\ q_2 \end{Bmatrix} \tag{12}$$

The transformation on the forces ($T_M^T T_{\Lambda_g}^T$) is premultiplied to the aerodynamic forces due to the trailing-edge flap. All of the aerodynamic forces must be transformed from the midchord to the elastic axis using Eq. (5).

C. Modeling of the Anisotropic Piezoelectrics

Three factors govern the effectiveness of anisotropic piezoelectric actuators: 1) their authority, 2) anisotropy, and 3) orientation. Three appropriate normalizing parameters are first identified, followed by a derivation of a model for the equivalent piezoelectric force and moment acting on the typical section.

The piezoelectric authority scaling parameter is derived from the governing equation for a plate with induced strain actuation [Eq. (1)]. A simplified bending model is

$$D_{11}\frac{\partial^4 w}{\partial x^4} + \frac{\partial^2 m_{\Lambda_{11}}}{\partial x^2} = 0 \tag{13}$$

Nondimensionalizing the spanwise dimension x by the span l, the vertical displacement w by a reference displacement w_0, the substrate stiffnesses D_{ij} by a reference stiffness D_0, and the piezoelectric moment terms $m_{\Lambda_{ij}}$ by a reference moment m_{Λ_0} yields

$$\bar{D}_{11}\frac{\partial^4 \tilde{w}}{\partial \tilde{x}^4} + \frac{m_{\Lambda_0} l^2}{D_0 w_0}\frac{\partial^2 m_{\tilde{\Lambda}_{11}}}{\partial \tilde{x}^2} = 0 \tag{14}$$

where the tildes indicate nondimensional quantities. The new nondimensional group is

$$C_r = m_{\Lambda_0} l^2/D_0 w_0 \tag{15}$$

Note that, increasing the piezoelectric thickness does not monotonically increase C_r since the piezoelectric stiffness affects both m_{Λ_0} and D_0. Holding the substrate thickness constant, Fig. 3 shows the effect of increasing thickness ratio on C_r. Isotropic piezoelectrics and a fiber sweep angle of -30 deg are assumed.

Both the bending and bend-twist curves show a maximum in C_r for increasing piezoelectric thickness, derived here for a solid composite plate with piezoelectrics added to the top and bottom surfaces. The thickness ratio is defined as the ratio of the thickness of the piezoelectric on one side of the plate to the structural thickness. The reference stiffnesses for the bending and bend-twist cases, respectively, are

$$\begin{aligned} D_0 &= D_{11} \\ D_0 &= \frac{D_{11}D_{66} - D_{16}^2}{D_{16}} \end{aligned} \tag{16}$$

The reference bending stiffness is the obvious choice and the reference bend-twist stiffness may be obtained by assuming only a spanwise bending moment and calculating the resulting twist curvature. It may also be derived from the typical section model by representing a bending moment by a force applied at the midchord and solving Eq. (6) for $\bar{\alpha}_{EA}$.

For the bending case, the authority parameter initially increases because the piezoelectric moment m_Λ increases as the piezoelectric thickness is increased from zero. However, the piezoelectric contribution to the stiffness is also increasing. When the piezoelectric stiffness begins to dominate the overall stiffness, the piezoelectric authority decreases; this is because the piezoelectric stiffness is proportional to the cube of the piezoelectric thickness, while the piezoelectric moment is only proportional to the square of the piezoelectric thickness.

In addition to the moment and stiffness effects, the bend-twist authority is also influenced by the relative isotropy of the piezoelectric to the substrate. If elastically isotropic piezoelectrics are assumed, the overall bend-twist coupling (D_{16}) of the structure is decreased as the piezoelectric thickness is increased. It should be noted that the location of the maximum for both curves is also dependent on the ratio of piezoelectric stiffness to substrate stiffness and the magnitude of

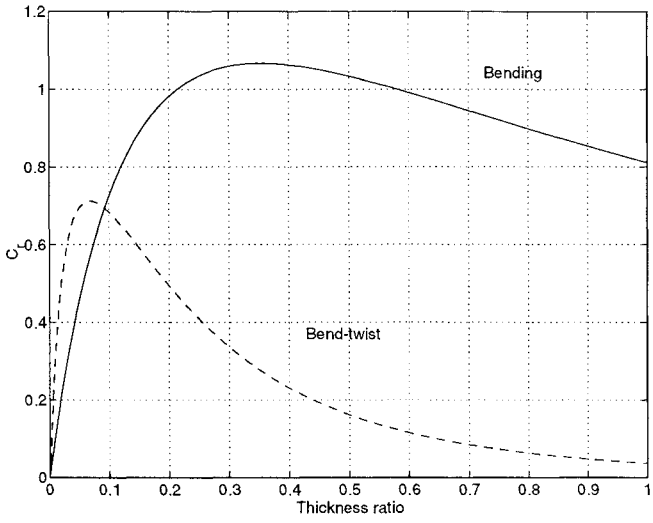

Fig. 3 Variation in the piezoelectric authority parameter for increasing thickness ratio. $w_0 = b$.

the curves is dependent on the geometric parameters in C_r, but the presence of the maxima is fundamental.

The significance of this new nondimensional parameter is twofold. First, it can be used to compare the relative piezoelectric authority of two wings (e.g., a model and full-scale wing). Second, the actual value of the parameter provides an indication of the level of piezoelectric authority. As a reference, for a cantilever beam actuated in bending by a uniformly distributed piezoelectric layer, the tip deflection created by $C_r = 1$ is $0.5w_0$ or half the reference displacement.

For piezoelectrics with induced strain anisotropy, two additional parameters are required: 1) the induced strain anisotropy d_r, and 2) the angle at which the piezoelectric principle axes are placed with respect to the wing axes θ_p. The piezoelectric in-plane actuation strains are

$$\begin{Bmatrix} \hat{\Lambda}_1 \\ \hat{\Lambda}_2 \end{Bmatrix} = \begin{Bmatrix} d_{31} \\ d_{32} \end{Bmatrix} E_3 = \begin{Bmatrix} 1 \\ d_r \end{Bmatrix} d_{31} E_3 \tag{17}$$

Using the actuation strain vector and the appropriate material stiffness matrix for the piezoelectrics, assumed to be elastically in-plane orthotropic, the stresses induced by the piezoelectrics are calculated. These stresses are then transformed using the two-dimensional tensor transformation from the piezoelectric principle axes (at θ_p) to the wing structural axes. The piezoelectric modal forces, F_{Λ_1} and F_{Λ_2}, which correspond to q_1 and q_2, may be calculated using the Ritz method. These piezoelectric modal forces must be further transformed to the elastic axis coordinates [Eq. (5)] and divided by the span to be incorporated into the typical section equations:

$$\begin{Bmatrix} \bar{F}_{\Lambda_{EA}} \\ \bar{M}_{\Lambda_{EA}} \end{Bmatrix} = \frac{1}{\bar{l}} T_{EA}^T \begin{Bmatrix} \bar{F}_{\Lambda_1} \\ \bar{F}_{\Lambda_2} \end{Bmatrix} \tag{18}$$

In the following analyses, three different piezoelectric "actuators" are compared. The baseline case is a completely isotropic piezoelectric that has identical piezoelectric coverage on the top and bottom surfaces of the plate. The piezoelectrics are actuated in a bender configuration with the bottom piezoelectric's induced strain being the opposite of the top's strain. The remaining two cases utilize the piezoelectric anisotropy. In both cases, the major axis of the top piezoelectric is oriented at θ_p and the major axis of the bottom piezoelectric is oriented at $-\theta_p$ (Fig. 2). The second actuator is referred to as the bend actuator and is actuated in a bender configuration. On an isotropic structure, this actuator induces bending and extension. The third actuator is referred to as the twist actuator and has both piezoelectrics actuated with the same strain. This actuator induces torsion and extension on an isotropic structure. The extension effects of these actuators are ignored in the typical section model.

The force and moment at the elastic axis caused by the bend actuator are

$$\begin{aligned} \bar{F}_{\Lambda_{EA}} &= \frac{8h_p t_p \hat{\Lambda}_1 \bar{b}}{\bar{l}_{ts}^2} [(\hat{Q}_{11} + d_r \hat{Q}_{12})\cos^2\theta_p \\ &\quad + (\hat{Q}_{12} + d_r \hat{Q}_{22})\sin^2\theta_p] \\ \bar{M}_{\Lambda_{EA}} &= \frac{-8h_p t_p \hat{\Lambda}_1 a \bar{b}^2}{\bar{l}_{ts}^2} [(\hat{Q}_{11} + d_r \hat{Q}_{12})\cos^2\theta_p \\ &\quad + (\hat{Q}_{12} + d_r \hat{Q}_{22})\sin^2\theta_p] \end{aligned} \tag{19}$$

where h_p is the height from the neutral axis to the midline of the piezoelectric, t_p is the thickness of the piezoelectric, $\hat{\Lambda}_j$ is the piezoelectric actuation strain, $\hat{Q}_{ij}$ is the piezoelectric modulus, and ($\hat{}$) indicates quantities in the piezoelectric axes. The expressions simplify if the piezoelectrics are elastically isotropic and their stiffness is determined only by $\hat{Q}_{11}$ and ν. The expressions for force and moment at the elastic axis are further simplified for actuators isotropic in both their elastic and induced-strain properties ($d_r = 1$). Note that the actuators produce only a force at the midchord. The presence of a moment is due to the displacement of the elastic axis from the midchord.

In contrast, the twist actuator creates a pure moment:

$$\begin{aligned} \bar{F}_{\Lambda_{EA}} &= 0 \\ \bar{M}_{\Lambda_{EA}} &= \frac{8h_p t_p \hat{\Lambda}_1 b}{l_{ts}} [\hat{Q}_{11} + \hat{Q}_{12}(d_r - 1) - d_r \hat{Q}_{22}]\sin\theta_p \cos\theta_p \end{aligned} \tag{20}$$

As before, the expressions simplify for elastically isotropic actuators. If the piezoelectrics of the twist actuator are made isotropic in their elastic and induced strain properties ($d_r = 1$) the moment goes to zero as well.

III. Wing Model Parameters and Passive Aeroelastic Analysis

In order to have a concrete example for calculation, a simple wing model is studied. The wing model is a uniform rectangular plate with the following parameters: material AS1/3501-6, AR based on semispan of 4, thickness ratio of 1%, and piezoelectric thickness ratio of 0.03. The further simplification that all plies are at an angle of θ_f (Fig. 2) is made. PZT-5H piezoelectric is assumed to cover both sides of the laminate with a bending $C_r = 0.16$ for a $\theta_f = -30$ and $w_0 = b$. This piezoelectric thickness is chosen to simulate a MIT/NASA wind-tunnel model being tested in the Langley Transonic Dynamics Tunnel.[12] Fiber sweep angle θ_f refers to the angle of the composite fibers from the structural reference axis, and the piezoelectric angle θ_p refers to the angle of the piezoelectric major axis from the structural reference axis.

Using this wing, the relationship between fiber sweep angle and elastic axis location can be derived explicitly for the bare laminate and the laminate with piezoelectrics (Fig. 4). The angle at which the maximum bend-twist coupling and excursion of the elastic axis is achieved is lower for the case with piezoelectrics. The added isotropy of the piezoelectrics lessens the overall bend-twist coupling of the structure. In both cases, the displacement of the elastic axis from the midchord increases essentially linearly until nearly the angle of maximum displacement. Past this angle, increasing the fiber sweep angle decreases the elastic axis displacement up to a fiber sweep angle of 90 deg, at which there is once again no bend-twist coupling. Laminate strength characteristics would place an upper limit on the allowable fiber angle for any physical wing.

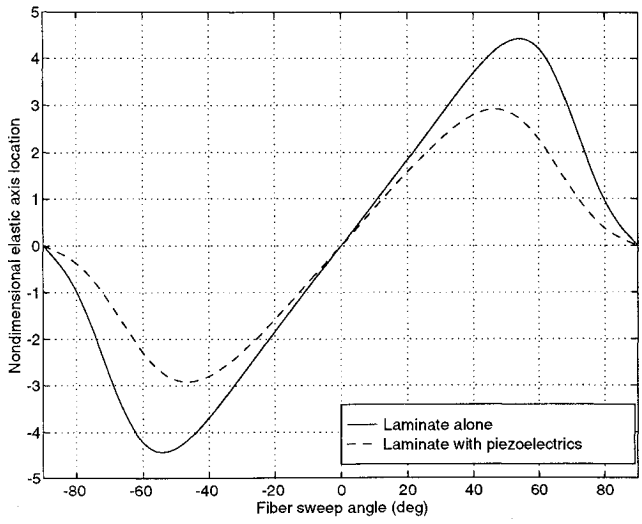

Fig. 4 Movement of elastic axis for varying fiber sweep angle; *ab* is the distance of the elastic axis aft of the midchord, where *b* is the semichord.

The nature and speed of the first aeroelastic instability predicted by the hybrid Ritz-typical section matches the experimental data from Landsberger and Dugundji well.[5] For the common case of aft geometric sweep and forward (in structural coordinates) fiber sweep, the flutter speed is relatively insensitive to these two parameters and they can be optimized for piezoelectric authority without dramatically altering the passive characteristics of the model.

IV. Comparisons of Open-Loop Authority

Before designing controllers, a static open-loop analysis is performed to evaluate the effectiveness of the various actuators. As an indication of effectiveness, the typical section equations are solved for the nondimensionalized plunge and pitch displacements.

To enhance understanding of the various coupling mechanisms, the following analysis uses a sequential approach. First, comparisons of the isotropic, bend, and twist piezoelectric actuators are made for zero airspeed. Then unswept aerodynamics are added, and finally the aerodynamic coupling associated with geometric sweep is included. For nonzero airspeed below divergence, the effectiveness of a flap that is 10% of the chord is also included. For clarity, the bend and twist piezoelectric actuators use piezoelectrics that ideally induce anisotropic strain ($d_r = 0$), but are elastically isotropic. The authority of an actuator with an intermediate anisotropic strain ratio (e.g., $d_r = 0.5$) lies between that of the ideally anisotropic and the isotropic.

Examining the nondimensional static displacements at zero airspeed provides a clear view of the effects of fiber sweep angle and piezoelectric angle on the effectiveness of the various piezoelectric actuators. The displacement caused by the piezoelectrics is a product of the piezoelectric force and moment and the stiffness of the overall structure. Equations (19) and (20) show that the fiber sweep angle does not affect the piezoelectric force and moment at the elastic axis. For an elastically isotropic actuator, the piezoelectric angle does not affect the stiffnesses. This implies that the effect of the fiber sweep angle and the effect of the piezoelectric angle are largely separable when the piezoelectrics are elastically isotropic: the fiber sweep angle affecting only the stiffness matrix, and the piezoelectric angle affecting only the piezoelectric force and moment. Therefore, the effects of varying the angles may be examined individually. A piezoelectric angle of 45 deg is chosen for the fiber angle study because it optimizes the twist actuator's authority. A representative fiber angle of -30 deg is chosen for the piezoelectric angle study.

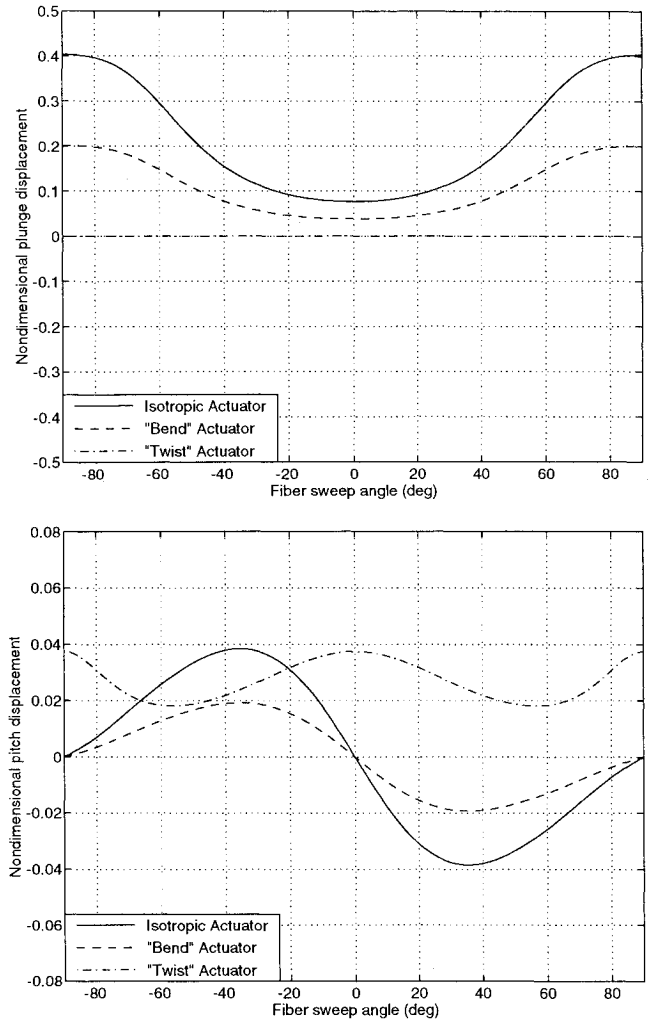

Fig. 5 Open-loop effectiveness without aerodynamics for varying fiber sweep angle. Piezoelectric angle is 45 deg.

The effect of fiber sweep angle on the piezoelectric authority is due solely to the variation in stiffnesses (Fig. 5). The isotropic and bend piezoelectric actuators vary in their effectiveness over the plunge displacement according to the spanwise stiffness. With a fiber angle of 0 deg, the structure has its maximum spanwise stiffness and, therefore, the actuators have their minimum authority. As the fiber angle increases to 90 deg, the spanwise stiffness decreases and the piezoelectric authority increases. The isotropic actuator is more effective than the bend actuator because of the Poisson's effect of the strain in the chordwise direction, since no chordwise bending is permitted. The twist actuator demonstrates no authority over the plunge displacement since it commands no force, and the stiffness matrix without aerodynamics is uncoupled. It should be noted that C_r changes with varying fiber sweep.

The three actuators provide fairly equivalent levels of pitch displacement. The twist actuator's variation with fiber angle is due to the torsional stiffness variation. When the torsional stiffness is highest (e.g., a fiber sweep angle of 45 deg) the twist actuator's torsional authority is lowest. The reverse is also true. The isotropic and bend actuators gain torsional authority strictly through the bend-twist coupling of the structure. Their authority over the pitch displacement is proportional to the elastic axis location and inversely proportional to the torsional stiffness. The dominant effect is that of the elastic axis, which can be seen by comparing Fig. 5 with Fig. 4. The slight shift in the peak is caused by the torsional stiffness variation. When there is no bend-twist coupling (i.e., a

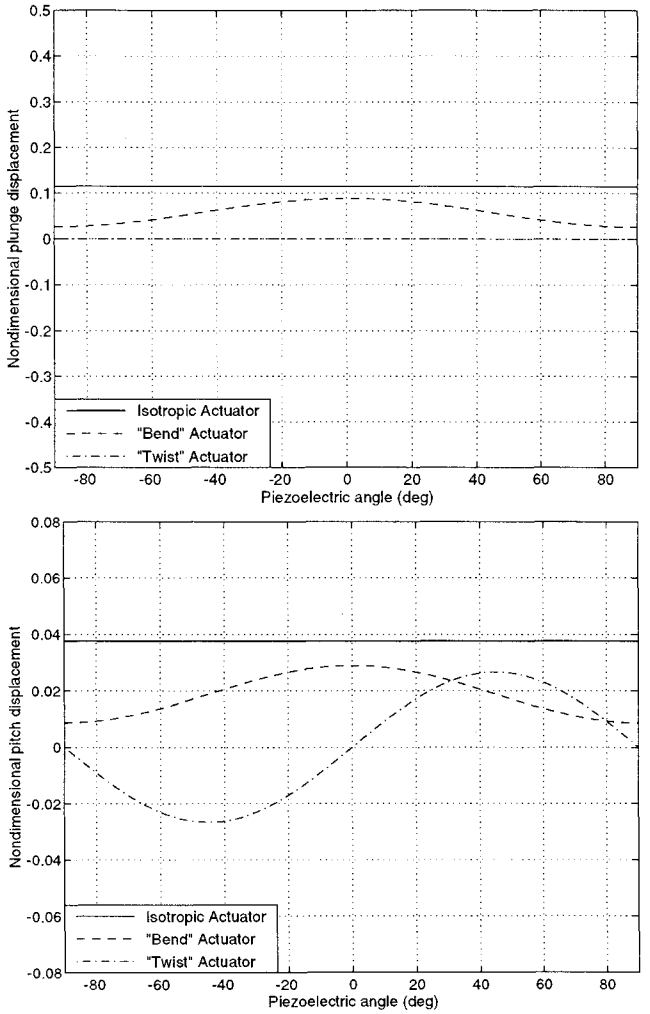

Fig. 6 Open-loop effectiveness without aerodynamics for varying piezoelectric angle. Fiber sweep angle is −30 deg.

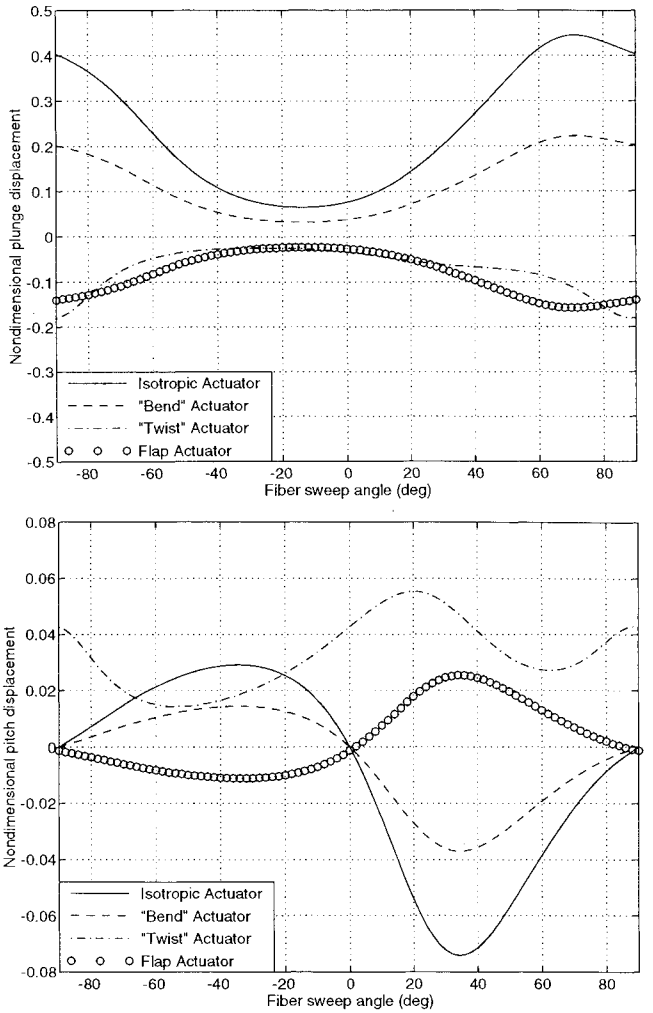

Fig. 7 Open-loop effectiveness with aerodynamics for varying fiber sweep angle. Piezoelectric angle is 45 deg. Flap angle is 5 deg. No geometric sweep.

fiber angle of 0 deg) the isotropic and bend actuators have no authority over the torsional motion.

The variation in open-loop effectiveness due to the piezoelectric angle can be seen in Fig. 6. The twist actuator exhibits the sin θ_p cos θ_p behavior of Eq. (20) in its pitch authority. The bend actuator is most effective when the piezoelectrics are aligned with the wing axis, since the bend actuator derives all of its effect, whether pitch or plunge, from bending the wing. Therefore, it is most effective in twist when concentrating its efforts on spanwise bending. The isotropic actuator's effectiveness does not vary with piezoelectric angle and is shown for reference only.

A parallel comparison of the static aeroelastic characteristics is made with unswept aerodynamics included (Fig. 7). An airspeed of three-quarters of the lowest divergence speed is used guaranteeing that the model is not near static divergence for any fiber angle. The trailing-edge flap effectiveness is also included in Fig. 7.

The incorporation of unswept aerodynamics adds two effects to the trends of Figs. 5 and 6: it alters the effective torsional stiffness and introduces twist-bend coupling. The first effect is most clearly seen in the asymmetry of the pitch displacement curves in Fig. 7. When the elastic axis location is aft of the c.p., the aerodynamics decrease the torsional stiffness and increase the actuator authority. Since the c.p. is located at the quarter-chord point, it can be seen from Fig. 4 that the region of decreased torsional stiffness covers essentially the right half of Fig. 7. On the other hand, when the elastic axis is forward of the c.p., the torsional stiffness is increased and the actuator authority decreased, as seen in the left half of Fig. 7.

Examining the plunge displacement curves, the dominant trend is still the variation of the bending stiffness. The asymmetry with respect to θ_f is due to the twist-bend coupling created by the lift force. The coupling is proportional to the lift force and inversely proportional to the bending stiffness and the effective torsional stiffness. The contribution of the torsional stiffness causes the asymmetry, again favoring the aft (positive) fiber sweep angles. In addition, the coupling allows the twist actuator control of the plunge displacement.

The trailing-edge flap resembles the isotropic and bend piezoelectric actuators (see Fig. 7). Both its plunge authority and its pitch authority resemble that of the isotropic and bend piezoelectric actuators. The pitch authority is gained through the bend-twist coupling and the plunge authority shows the same dependence as the isotropic and bend actuators on the spanwise bending stiffness. The effect of the aerodynamic coupling on the flap authority parallels the effect on the isotropic and bend actuators' authority.

The final coupling is the introduction of geometric sweep (Fig. 8). The same airspeed is used with a representative geometric sweep angle of 30 deg. There are two differences of note between the cases without geometric sweep (Fig. 7) and those with it. First, adding the geometric sweep lessens the variation in the plunge displacement authority due to varying fiber sweep angle. Second, the asymmetry has been reduced. Aft geometric sweep creates the same "washout"

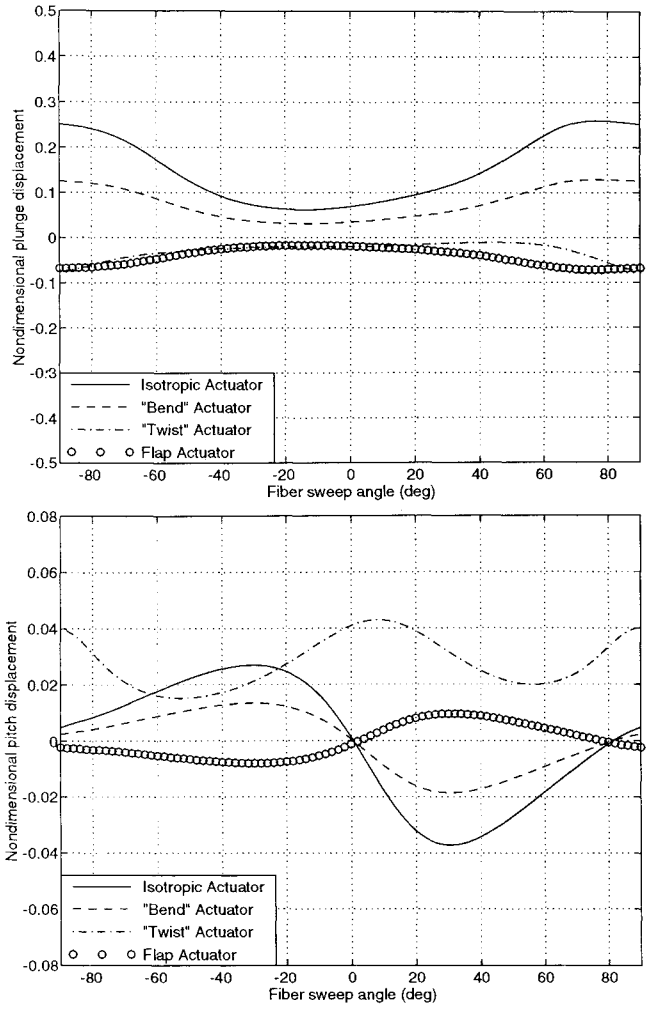

Fig. 8 Open-loop effectiveness with aerodynamics for varying fiber sweep angle. Piezoelectric angle is 45 deg. Flap angle is 5 deg. Geometric sweep angle is 30 deg.

effect as forward (negative) fiber sweep; this counteracts the effect of aft (positive) fiber sweep. Therefore, the torsional stiffness is not decreased as significantly as in the unswept case, and the actuator authority is not increased as significantly. The actuator effectiveness trends for varying piezoelectric angles are not affected by geometric sweep and are not shown.

V. Closed-Loop Comparisons

The final analysis involves designing closed loop controllers with the isotropic, bend, and twist piezoelectric actuators, the trailing-edge flap, and a combination bend and twist actuator. Both of the anisotropic piezoelectric actuators use their optimal piezoelectric angle: 0 deg for the bend actuator, and 45 deg for the twist actuator. The fiber angle is −30 deg. The method used to design the controllers is the linear quadratic regulator (LQR) method that assumes full state feedback.

The linear quadratic regulator method minimizes the following cost functional:

$$J = \int (\boldsymbol{x}^T Q \boldsymbol{x} + \rho \boldsymbol{u}^T R \boldsymbol{u})\, \mathrm{d}t \tag{21}$$

where $\boldsymbol{x}$ is the state vector and $\boldsymbol{u}$ is the control vector in a state–space representation. Q is the state weighting matrix, R is the control weighting matrix, and ρ is the control weighting. Letting ρ approach zero, "cheap" control, allows the system to use large amounts of control. Letting ρ approach infinity, "expensive" control, prohibits the system from using more control than is necessary to stabilize the plant. The nondimensional plunge and pitch displacements are equally weighted in the state weighting matrix. The control weighting matrix normalizes the controls by their assumed maximums: $300\mu\varepsilon$ for the strain actuators and 5 deg for the trailing-edge flap.

The state cost and control cost of each actuator are calculated and their relationship plotted. The costs are functions of the state covariance due to the disturbance. A 1 deg^2/Hz broadband white noise angle-of-attack disturbance is chosen to resemble a gust disturbance. The state cost is the weighted covariance of the states and the control cost is the weighted covariance of the commanded controls. The weighting matrices are the same as those used in the LQ cost function.

One of the great advantages of using piezoelectric actuators is that multiple actuator combinations can be designed using the same set of piezoelectrics. The "combination" actuator allows effective control of both modes of the typical section. In this case, both the twist piezoelectric actuator and the bend piezoelectric actuator can be implemented using one set of piezoelectrics. This combination is implemented electrically by superimposing the signals on top of one another. To ensure that the total strain in each piezoelectric does not exceed maximum, the maximum strain for each actuator would need to be half of the maximum strain for a single actuator acting alone, or $150\mu\varepsilon$. Since only one physical set of piezoelectric is used, only one piezoelectric angle may be selected. For this analysis, a piezoelectric angle of 45 deg is selected since it optimizes the twist actuator's performance.

The cost curve analysis shows the limitations of single actuators (Fig. 9). For a nonsquare system in which there are fewer inputs than performance variables, there is a fundamental performance limit, and the state cost cannot be driven to zero.[13] This is evidenced by the horizontal asymptotes for high control cost of all of the single actuators. The combination actuator, being a square system, does not have such a limit and can drive the state cost to zero.

The relative performance of the various actuators may also be seen in the cost curves. The disturbance excites the plunge state more than the pitch state. The best plunge actuators, the isotropic and bend actuators, perform the best of the single actuators in the high control cost region. In the low control cost region, the twist actuator has the lowest state cost. For low control costs, the twist actuator is able to add significant damping to the second mode, and add some damping to the first mode. In the same control cost region, the other three actuators are completely unable to damp the second mode. Since both modes are weighted in the performance, these actuators do not perform as well for low control effort. It is

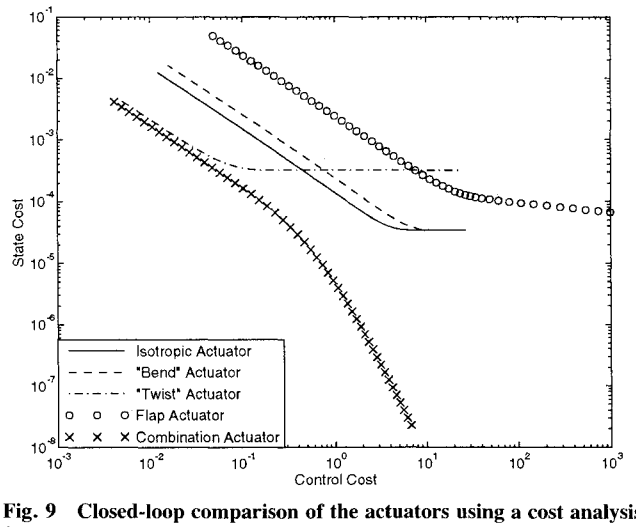

Fig. 9 Closed-loop comparison of the actuators using a cost analysis for a white-noise angle-of-attack disturbance.

only at higher control costs that they are able to damp the second mode and improve their relative performance. The combination actuator provides the best performance of all actuators in all control regions, demonstrating the importance of having effective control of both modes.

VI. Conclusions

This article provides a foundation for understanding the piezoelectric authority optimization problem in aeroelastic control. Specifically, the three different coupling mechanisms available to provide piezoelectric twist control in addition to plunge control are examined. The effects of an anisotropic laminate, swept aerodynamics, and anisotropic piezoelectrics have been successfully implemented in a typical section model. To first order, these three effects are separable and uncoupled.

Initially, the passive aeroelastic behavior was examined. The typical section model created predicts the qualitative aeroelastic stability trends. From these trends, regions may be found in which the passive aeroelastic behavior is relatively insensitive to changes in the fiber sweep angle. In these regions, fiber sweep angle can be used to modify the bend-twist coupling of the anisotropic laminate to optimize piezoelectric authority.

Adding the piezoelectrics, the appropriate nondimensional piezoelectric authority parameter C_r has been derived. This scaling parameter indicates that the piezoelectric authority does not increase monotonically for either bending or bend-twist control. Therefore, optimal values of C_r may be found for both bending and bend-twist control.

With the introduction of anisotropic piezoelectrics, there exist three distinct choices for piezoelectric aeroelastic actuators. Using isotropic piezoelectrics, the only workable option is a bending configuration, with the top piezoelectric actuated opposite the bottom piezoelectric. With the anisotropic piezoelectrics, two new possibilities arise. Placing the top and bottom piezoelectric actuators at equal and opposite angles from the midchord, the actuators may either be commanded together or oppositely. Commanding the actuators together acts as a twist actuator. Commanding them oppositely acts as a bend actuator much like the isotropic actuator.

From the modeling and open-loop analysis, it is shown that the dependence of the piezoelectric authority on the piezoelectric angle and the fiber angle are largely separable effects. The piezoelectric forcing term is dependent only on the piezoelectric angle, and the stiffness is dominated by the fiber angle for reasonable amounts of piezoelectric coverage. The bend-twist coupling is governed by the elastic axis location.

Both the open- and closed-loop analyses show that for single actuators the performance of the isotropic strain actuator coupled to an anisotropic laminate is comparable to an anisotropic actuator in either a bend or twist configuration. The single actuators all have a limit on performance at high control authority. All single piezoelectric actuators were better than the flap.

The closed loop analyses indicate that a combination piezoelectric actuator provides the best performance. The combination actuator is created by using one set of anisotropic piezoelectrics that are electrically commanded as both a bend and twist actuator. Conceptually similar combination actuators can be made with isotropic piezoelectric actuators by segmenting the piezoelectrics according to strain node lines for different modes. An added advantage of the induced strain actuators for aeroelastic control is this inherent ability to be electrically segmented in such a way as to eliminate the fundamental performance limitation of a single actuator.

Acknowledgments

This research effort was supported by NASA Cooperative Agreement NCC-1-157 with Jennifer Heeg serving as Program Monitor. In addition, C. Y. Lin was partially supported by a National Science Foundation Graduate Fellowship.

References

[1]Lazarus, K. B., Crawley, E. F., and Lin, C. Y., "Fundamental Mechanisms of Aeroelastic Control with Control Surface and Strain Actuation," *Proceedings of the AIAA 32nd Structures, Structural Dynamics, and Materials Conference*, AIAA, Washington, DC, 1991, pp. 1817–1831 (AIAA Paper 91-0985).

[2]Lazarus, K. B., and Crawley, E. F., "Multivariable High-Authority Control of Plate-Like Active Structures," *Proceedings of the AIAA 33rd Structures, Structural Dynamics, and Materials Conference*, AIAA, Washington, DC, 1992, pp. 931–945 (AIAA Paper 92-2529).

[3]Heeg, J., "An Analytical and Experimental Investigation of Flutter Suppression via Piezoelectric Actuation," *Proceedings of the AIAA Dynamics Specialists Conference*, AIAA, Washington, DC, 1992, pp. 237–247 (AIAA Paper 92-2106).

[4]Lin, C. Y., and Crawley, E. F., "Design Considerations for a Strain Actuated Adaptive Wing for Aeroelastic Control," *Proceedings of the 4th International Conference on Adaptive Structures* (Cologne, Germany), Technomic, Lancaster, PA, 1993, pp. 542–556.

[5]Landsberger, B. J., and Dugundji, J., "Experimental Aeroelastic Behavior of Unswept and Forward-Swept Cantilever Graphite/Epoxy Wings," *Journal of Aircraft*, Vol. 22, No. 8, 1985, pp. 679–686.

[6]Weisshaar, T. A., and Ryan, R. J., "Control of Aeroelastic Instabilities Through Stiffness Cross-Coupling," *Journal of Aircraft*, Vol. 23, No. 2, 1986, pp. 148–155.

[7]Hagood, N. W., and Bent, A. A., "Development of Piezoelectric Fiber Composites for Structural Actuation," *Proceedings of the AIAA 33rd Structures, Structural Dynamics, and Materials Conference*, AIAA, Washington, DC, 1993, pp. 3625–3638 (AIAA Paper 93-1717).

[8]Hagood, N., Kindel, R., Ghandi, K., and Gaudenzi, P., "Improving Transverse Actuation of Piezoceramics Using Interdigitated Surface Electrodes," *Proceedings, Smart Structures and Materials 1993: Smart Structures and Intelligent Systems*, SPIE, Bellingham, WA, 1993, pp. 341–352 (SPIE 1917).

[9]Barrett, R., "Active Plate and Wing Research Using EDAP Elements," *Smart Materials and Structures*, Vol. 1, No. 3, 1992, pp. 214–226.

[10]Ehlers, S. M., and Weisshaar, T. A., "Adaptive Wing Flexural Control," *Proceedings of the 3rd International Conference on Adaptive Structures* (San Diego, CA), Technomic, Lancaster, PA, 1992, pp. 28–40.

[11]Jones, R. M., *Mechanics of Composite Materials*, Hemisphere, New York, 1975.

[12]Lin, C. Y., and Crawley, E. F., "Strain Actuated Aeroelastic Control," TR 2-93, Massachusetts Inst. of Technology Space Engineering Research Center, Cambridge, MA, Feb. 1993.

[13]Kwakernaak, H., and Sivan, R., "The Maximally Achievable Accuracy of Linear Optimal Regulators and Linear Optimal Filters," *IEEE Transactions on Automatic Control*, Vol. AC-17, No. 1, 1972, pp. 79–86.